Geophysical Journal International

Geophys. J. Int. (2020) **222,** 956–964
Advance Access publication 2020 May 9
GJI Seismology

doi: 10.1093/gji/ggaa224

XKS splitting-based upper-mantle deformation in the Jiaodong Peninsula records the boundary between the North China Craton and South China Block

Chenglong Wu,[1] Tao Xu,[1,2] Yinshuang Ai,[2,3] Weiyu Dong[1,4] and Long Li[3,4]

[1]*State Key Laboratory of Lithospheric Evolution, Institute of Geology and Geophysics, Chinese Academy of Sciences, Beijing* 100029*, China. E-mail: xutao@mail.iggcas.ac.cn*
[2]*CAS Center for Excellence in Tibetan Plateau Earth Sciences, Beijing* 100101*, China*
[3]*Key Laboratory of Earth and Planetary Physics, Institute of Geology and Geophysics, Chinese Academy of Sciences, Beijing* 100029*, China*
[4]*University of Chinese Academy of Sciences, Beijing* 100049*, China*

Accepted 2020 May 5. Received 2020 May 5; in original form 2020 January 15

SUMMARY

The Jiaodong Peninsula consists of the Jiaobei massif and the Northern Sulu UHP massif. These are separated by the Wulian suture zone (WSZ), a key region for understanding the collision between the North China Craton (NCC) and South China Block (SCB). To interpret this collisional zone, a broad-band seismic profile of 20 stations was installed across the WSZ. Shear wave splitting analysis of teleseismic data revealed a contrast in the splitting patterns beneath different structural zones of the Jiaodong Peninsula. The anisotropic structures of the Jiaobei massif and Northern Sulu UHP massif can be explained by a single anisotropic layer model with WNW-ESE or E-W oriented fast directions. In the WSZ, splitting parameters exhibit pronounced variation in backazimuths indicating a two-layer anisotropy pattern. The lower layer exhibits a WNW-ESE fast direction consistent with that observed in the other two regions. Because the fast direction is generally parallel to the present-day direction of Pacific plate subduction, the anisotropy most likely represents asthenospheric return flow in the big mantle wedge caused by Pacific plate subduction. The upper layer exhibits an NE fast direction, that is, parallel to faulting associated with the WSZ. The lithosphere may preserve fossilized anisotropy induced by the Late Triassic collision of the NCC and SCB even after subsequent destruction and thinning from the Late Mesozoic to Cenozoic. We infer that the WSZ represents a lithospheric-scale structural boundary between the NCC and SCB.

Key words: Seismic anisotropy; Fractures, faults, and high strain deformation zones; Rheology: mantle.

1 INTRODUCTION

The boundary between the North China Craton (NCC) and the South China Block (SCB) records continental subduction and tectonic processes of Northeast Asia. During the Late Triassic, northward subduction of the SCB beneath the NCC generated the Dabie-Sulu UHP orogenic belt, which extends over 1500 km in an E-W orientation and represents an irregular suture between the NCC and SCB (Liou *et al.* 1996; Hacker et al., 1998, 2000). The suture west of the Tan–Lu Fault (TLF) lies near the northern boundary of the Qinling–Dabie orogenic belt (Okay & Celal Sengo¨r 1992). The belt and the suture in this location are abruptly truncated to the east by the NNE-striking TLF (Fig. 1).

The location of the suture east of the TLF remains uncertain. The Wulian suture zone (WSZ) is commonly interpreted to represent the boundary between the NCC and SCB in the Jiaodong Peninsula east of the TLF (Cao *et al.* 1990; Okay & Celal Sengo¨r 1992; Yin & Nie 1993; Gilder *et al.* 1999; Zhai *et al.* 2000; Zhou *et al.* 2008). The WSZ separates the Northern Sulu UHP massif in the southeast, which is composed of typical UHP metamorphic rocks, from the Jiaobei massif in the northwest, which consists of both Precambrian basement and Mesozoic magmatic rocks (Fig. 1). A crustal-detachment model proposed by Li (1994) however interpreted the upper crust of the SCB as detached from the lower crust and thrust over the NCC for more than 400 km. This model also interpreted the lower part of the lithosphere as subducted under the NCC along a subsurface suture running east from Nanjing. Structural analysis by Faure et al. (2001, 2002, 2003) indicated that the Jiaobei massif belongs to the SCB and that the boundary between the NCC and SCB must lie to the north of the Jiaodong Peninsula. Findings reported in Wu *et al.* (2004) and Zheng *et al.* (2005) that the Wulian granitoids represent tectonic slices scraped off from the

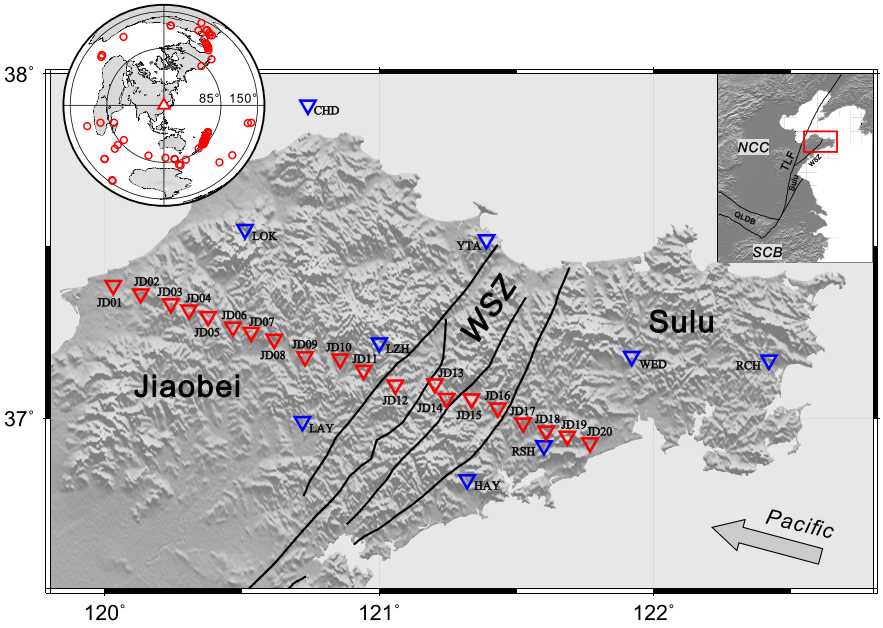

Figure 1. Map of the Jiaodong Peninsula (eastern China). The study area is noted by the red rectangle in the upper right inset. Enlarged view: the red triangles indicate the locations of the stations deployed along the seismic profile NCISP9. Blue triangles represent permanent stations. The grey arrow indicates the subduction direction of the Pacific plate. Earthquakes used for SWS analysis are shown as small red circles on a worldwide map in the upper left inset. The central triangle indicates the location of the study area. Abbreviations: Jiaobei, Jiaobei massif; Sulu, Northern Sulu UHP massif; WSZ, Wulian suture zone; in the upper right inset: NCC, North China Craton; SCB, South China Block; QLDB, Qinling–Dabie orogenic belt and TLF, Tan–Lu fault.

upper part of the SCB during Late Triassic continental subduction supported the interpretation that the suture lies north of the WSZ.

Collision between the NCC and SCB would cause lithospheric deformation along the boundary between them and thereby imprint the lithosphere with a crystallographic fabric as fossilized anisotropy (Silver & Chan 1988). Subsequent tectonic activity could disturb this fabric as could present-day asthenospheric flow. High-resolution seismic observations can detect upper-mantle deformation beyond the limitation of spatially confined geochemical samples. Mantle deformation can be specifically obtained by estimating azimuthal seismic anisotropy caused by lattice preferred orientation (LPO) of olivine in the upper mantle (Nicolas & Christensen 1987; Zhang & Karato 1995). Shear wave splitting (SWS) analysis is an effective tool for detecting and measuring this seismic anisotropy (Silver & Chan 1991; Silver 1996; Savage 1999). This report describes SWS results from 20 portable broad-band stations deployed across the WSZ with additional data from nine surrounding permanent stations (Fig. 1). The results provide new insights into upper-mantle deformation in the Jiaodong Peninsula and further elucidate the boundary between the NCC and SCB.

2 DATA AND METHODS

2.1 Data

The teleseismic data used in this study were recorded by the linear seismic profile NCISP9 operated from 2017 November to 2019 August. The profile ran NW-SE across WSZ and included 20 broad-band stations (Fig. 1). The profile spanned a total length of 170 km with an average station spacing of 9 km. In order to increase data coverage, we used additional recordings from nine nearby permanent stations belonging to the China National Seismic Network between from 2017 March to 2018 September (Zheng *et al.* 2010).

2.2 Seismic sensor orientation correction

Prior to SWS analysis, we inspected and corrected the sensor misorientation using *P*-wave particle motion (Fontaine *et al.* 2009; Niu & Li 2011; Wang *et al.* 2016; Scholz *et al.* 2017). This procedure prevents station misorientation from degrading SWS results. We selected earthquakes with magnitudes (M_w) $\geq$ 5.5 and epicentral distances of 5°–90° (Fig. 2) and filtered the data within a 0.02–0.2 Hz frequency band. The data were retained if their average signal-to-noise ratio (S/N) of horizontal components exceeded 3.0 and their eigenvalue ratio ($\lambda_{min}/\lambda_{max}$) ratio was less than 0.2 (for more details see Wang *et al.* 2016). Then we applied a transverse energy minimizing function (minT) to the horizontal waveform data to estimate sensor misorientations. For an assumed component azimuth, α, we first rotate the two horizontal components into radial and transverse directions with the theoretical backazimuth for each event. We then calculated the S/N-weighted summation of the normalized *P*-wave energy in the transverse component of all the events as:

$$E_T\ (\alpha) = \frac{\sum_{i=1}^{N} \omega_i E_T^i\ (\alpha)}{\sum_{i=1}^{N} \omega_i}.$$

In this expression, $E_T^i(\alpha)$ is the energy in the transverse component calculated within a manually selected time window for the *i*th event and N represents the number of events. The weight, ω_i, is the mean S/N of the two horizontal components where $\omega_i = 0.5\times(R_{i,\mathrm{BHN}}+R_{i,\mathrm{BHE}})$. We varied α across a 0°–180° range at increments of 1°. The misorientation angle is considered as the value for the azimuth α when the sum of the *P*-wave energy in the

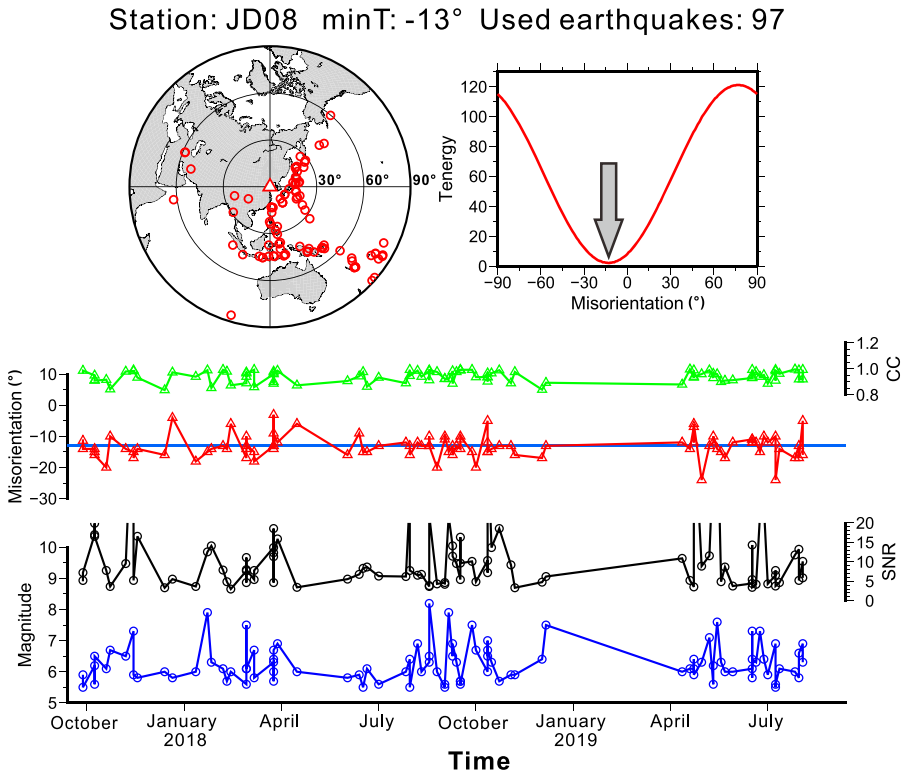

Figure 2. An example of the minT method applied to station JD08. Upper left plot: earthquakes used in analysis (small red circles on the global map) and the central triangle indicates the location of the study area. Lower graphics: single-earthquake minT measurements determined from 97 earthquakes and sorted by time (line linking red triangles), with reference to S/N (black line linking small circles) and the earthquake magnitude (blue line linking small circles). All these measurements are around the misorientation angle of −13°. The cross-correlation coefficients (CC) between the vertical and radial components are all close to 1.0 after misorientation correction (line linking green triangles). Upper right plot: variation curve of the Tenergy with the misorientation angle and the grey arrow points to the angle of −13° (clockwise from the north) corresponding to the minimum Tenergy.

transverse component $E_T(\alpha)$ (Tenergy) reaches its minimum value (Niu & Li 2011). In addition to station misorientation, the estimated misorientation angle may be also affected by a dipping interface or anisotropy (Schulte-Pelkum *et al.* 2001). However, the influence of a dipping interface or anisotropy is relatively small for misorientation estimates because they produce a periodic pattern with backazimuth (Wang *et al.* 2016). The misorientation angle for station JD08 was estimated at −13° clockwise from the north because the minimum Tenergy corresponds to this angle (upper right plot in Fig. 2). Each individual events gave misorientation angles estimated at around −13° (red triangles in Fig. 2). The green triangles indicate cross-correlation coefficients between vertical and radial components, which should approach 1.0 for good waveform quality. Misorientation angles for NCISP9 stations ranged from −18° to −1° with an average value of −9.6 ± 3.0° (Fig. S1 and Table S1, Supporting Information). Comparison with the mean magnetic declination −7.5° for the study region indicates that the misorientation angle arises mainly from inadequate correction of magnetic declination. Careful installation of temporary stations can give average misorientation angles of 3° from standard error sources (Wang *et al.* 2016). By contrast, permanent stations gave misorientation angles of around 0° (Fig. S1 and Table S1, Supporting Information).

The SWS analysis can be used to verify the accuracy of the sensor orientation correction. The SC and the RC methods generate consistent results in the absence of senor misorientation for the horizontal components (Tian *et al.* 2011; Wu *et al.* 2015). For uncorrected data, differences in fast directions calculated by the two methods exceeded 20° at station JD08 (Fig. 3). Misorientation correction reconciles measurements using these two methods (Fig. 4).

2.3 XKS splitting measurements

We selected earthquake events with magnitudes (M_w) ≥ 5.5 and epicentral distances ranging from 85° to 150° for SWS analysis. This study used a total of 68 events with broad azimuthal coverage (Fig. 1). Teleseismic SKS, SKKS and PKS phases were subjected to SWS analysis. The seismic data were bandpass filtered with corner frequencies of 0.04–0.5 Hz (Gao *et al.* 2010). We calculated SWS measurements using the Splitlab software (Wüstefeld *et al.* 2008). The rotation-correlation (RC) method (Bowman & Ando 1987) and the transverse-component minimization (SC) method (Silver & Chan 1991) were both utilized to obtain φ (fast-wave polarization direction) and δt (delay time) splitting parameters. SWS results were ranked based on the differences between the results generated by RC and SC (Wüstefeld & Bokelmann 2007). Ranking specifically used the angular difference $\Psi = |\varphi_{RC} - \varphi_{SC}|$ and the ratio of δt ($\rho = \delta t_{RC}/\delta t_{SC}$) to categorize results as good, fair and poor. 'Good' splitting measurements fall within the range of $0.8 \leq \rho \leq 1.1$ and $\Psi \leq 10°$, while 'fair' measurements fall within the range of $0.7 \leq \rho \leq 1.2$ and $\Psi \leq 15°$. All other splitting measurements categorized as 'poor'. Fig. 4 shows an example of a 'good' measurement of SKS phase generated by the event 2019:131:16:06 recorded at station JD08. Only good and fair measurements were advanced to

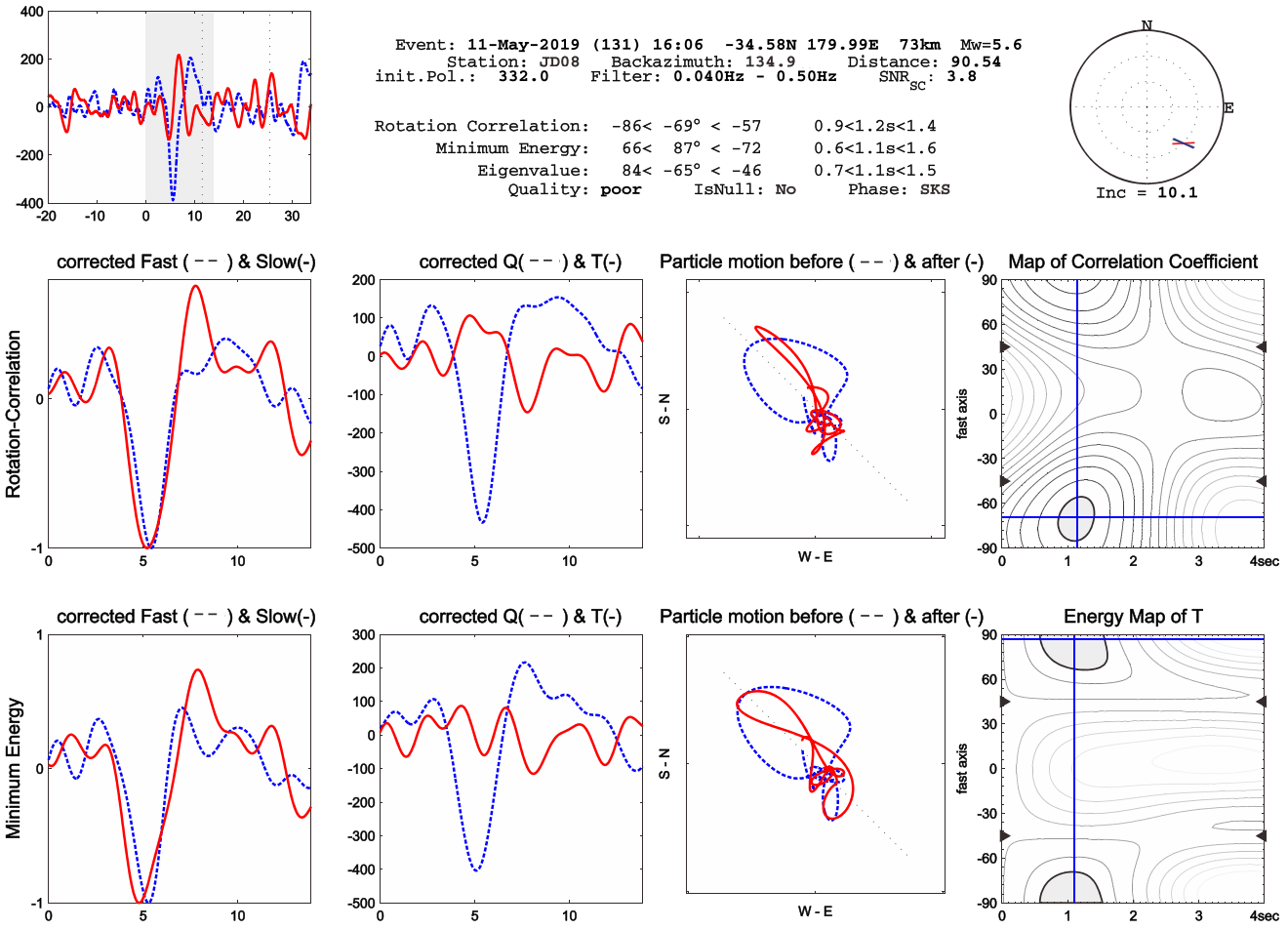

Figure 3. Example of SWS analysis for event 2019:131:16:06 recorded at station JD08 before sensor misorientation correction and processed using the Splitlab software package (Wüstefeld *et al.* 2008). Upper left panel shows the original radial and transverse seismic signals (blue dashed and red solid lines, respectively). The upper central panel gathers information about the event, station, filter, S/N, etc., and splitting results. The upper right panel is the stereoplot centred on the reference station. The middle and lower plots show the measurements obtained by applying the RC and the SC methods, respectively. From left to right: corrected fast and slow waveforms, radial (Q) and transverse (T) components once rotated, particle motion before and after anisotropy correction and contour diagram of splitting parameters pairs. The difference between the result obtained by the RC and the one provided by the SC method is over 20°.

further analysis. The transverse component contains no distinct energy when the backazimuth of the incoming wave ran parallel or perpendicular to the fast direction, or when the wave propagated through an isotropic media. This kind of measurements are null measurements defined as $32^\circ \leq \Psi \leq 58^\circ$ and $\rho \leq 0.3$ (Wu¨stefeld & Bokelmann 2007).

3 RESULTS

3.1 Spatial distribution of XKS splitting measurements

We obtained 90 splitting measurements including 72 'good' ones and 18 'fair' ones (as defined in Section 2.3 above, Fig. S2 and Table S3, Supporting Information) along with 124 null measurements (Fig. S3, Supporting Information). According to the distribution of the station locations, the results apply to three distinct spatial regions. Stations JD01–JD09, CHD, LOK, LAY and YTA were located within the Jiaobei massif. Although the splitting parameters at JD06 and JD07 showed some dependence on event backazimuths, we just calculated an average value due to the limited number of measurements. The average splitting parameters were $109 \pm 15^\circ$ for φ and 1.04 ± 0.26 s for δt. Stations JD10–JD17 and LZH were located on or adjacent to the WSZ, and their splitting parameters showed similar variation with backazimuth. This implies a complex anisotropic structure beneath the region being discussed below in Section 3.2. Stations JD18–20, RCH, WED, RSH and HAY occur within the Northern Sulu UHP massif and gave mean values of $\varphi = 95 \pm 16^\circ$ and $\delta t = 0.70 \pm 0.21$ s. Previous studies have reported SWS results for several permanent stations (Tian & Santosh 2015; Shi *et al.* 2015). Their station-averaged measurements gave E-W to WNW-ESE directions with a delay time of about 1.0 s. These values generally agree with our results (Table S2, Supporting Information).

3.2 Two-layer anisotropy structure in the WSZ

We combined results for stations within the WSZ due to limited measurements for stations in that region. The combined stations showed similar variation in backazimuth. A total of 35 pairs of splitting parameters showed strong azimuthal dependence with a $\pi/2$ periodicity suggesting a two-layer anisotropic structure with a horizontal axis of symmetry (Silver & Savage 1994). The complex anisotropy is also reflected in the null measurements for stations

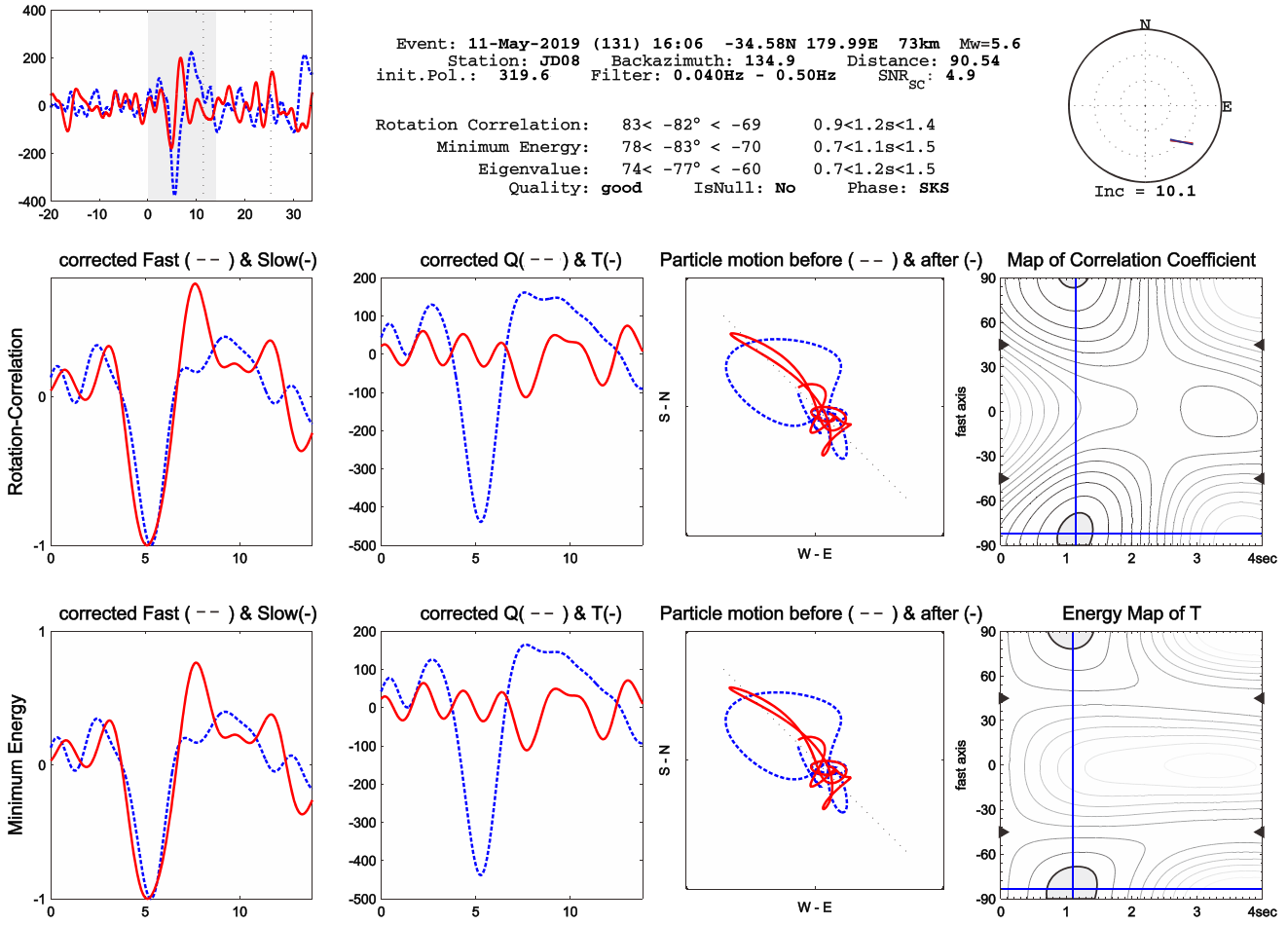

Figure 4. Same as in Fig. 3, but after sensor misorientation correction. Results obtained by the RC method and by the SC method show good agreement after this correction.

JD10 and JD15. These have varying backazimuths of incoming waves (Fig. S3, Supporting Information). We then calculated optimal splitting parameters for the two layers using a grid-search method. The fast direction for each layer was varied from 0° to 180° at 1° increments. The delay time was varied from 0 to 1.6 s at 0.1 s increments. We assumed that the delay time for the upper layer does not exceed half that for the lower layer based on the ∼70 km thickness of the lithosphere in the study region. Following statistical methods described in Walker *et al.* (2005) and Fontaine *et al.* (2007), we generated an *R* index to determine whether the two-layer models fit the splitting measurements better than a single-layer model with a horizontal symmetry axis. The *R* value should exceed 0.25 in order to meet statistical significance criteria and the maximum *R* gives the optimal pair of splitting parameters. The best-fitting model estimated here gave an *R* value of 0.39. This model included $\varphi_{\text{lower}} = 130°$, $\delta t_{\text{lower}} = 1.3$ s, $\varphi_{\text{upper}} = 54°$ and $\delta t_{\text{upper}} = 0.5$ s (Fig. 5). Fig. 5 also shows models with *R* values greater than 0.25. About 30 per cent of the valid models included parameters similar to those of the optimal model. Specifically, lower layer parameters ranged from $120° \leq \varphi_{\text{lower}} \leq 140°$ and 1.1 s $\leq \delta t_{\text{lower}} \leq 1.5$ s and upper layer parameters ranged from $44° \leq \varphi_{\text{upper}} \leq 64°$ and 0.3 s $\leq \delta t_{\text{upper}} \leq 0.7$ s. These limited ranges represent statistical support for the best-fitting solution. Fig. 6 shows the anisotropy results for both the one- and two-layer models. Tian *et al.* (2015) also detected two-layer anisotropy at three permanent stations in eastern China. The splitting parameters for the lower layer reported in their study agree with those reported here. However, fast directions for upper layers reported in Tian *et al.* (2015) approach an E-W direction, and delay times exceed those reported here. Distinct lithospheric deformation may generate different anisotropy estimates for the upper layer.

4 DISCUSSION

The SWS parameters depend on the travel path from the core mantle boundary to the station and therefore provide no direct constraints on the depth of anisotropy. It is broadly accepted that XKS splitting measurements mainly capture upper-mantle structure related to lithospheric deformation and/or asthenospheric flow (Silver 1996; Savage 1999; Long & van der Hilst 2005). According to receiver function analysis (Chen *et al.* 2006) and wide-angle reflection/refraction detection (Pan *et al.* 2015), the study area investigated here includes a lithosphere reaching only about 70 km thickness and a Moho depth of ∼33 km. Thus, the contribution from lithospheric deformation should be negligible compared to the average ∼1.0 s splitting time for the Jiaobei massif, Northern Sulu UHP massif and the lower layer of the WSZ (Table S2, Supporting Information). In addition, these regions exhibit E-W or WNW-ESE fast directions, which contrast the NE-oriented strike for surface structures in the study region (Fig. 6). We therefore interpret the single-layer anisotropy and lower layer of the two-layer

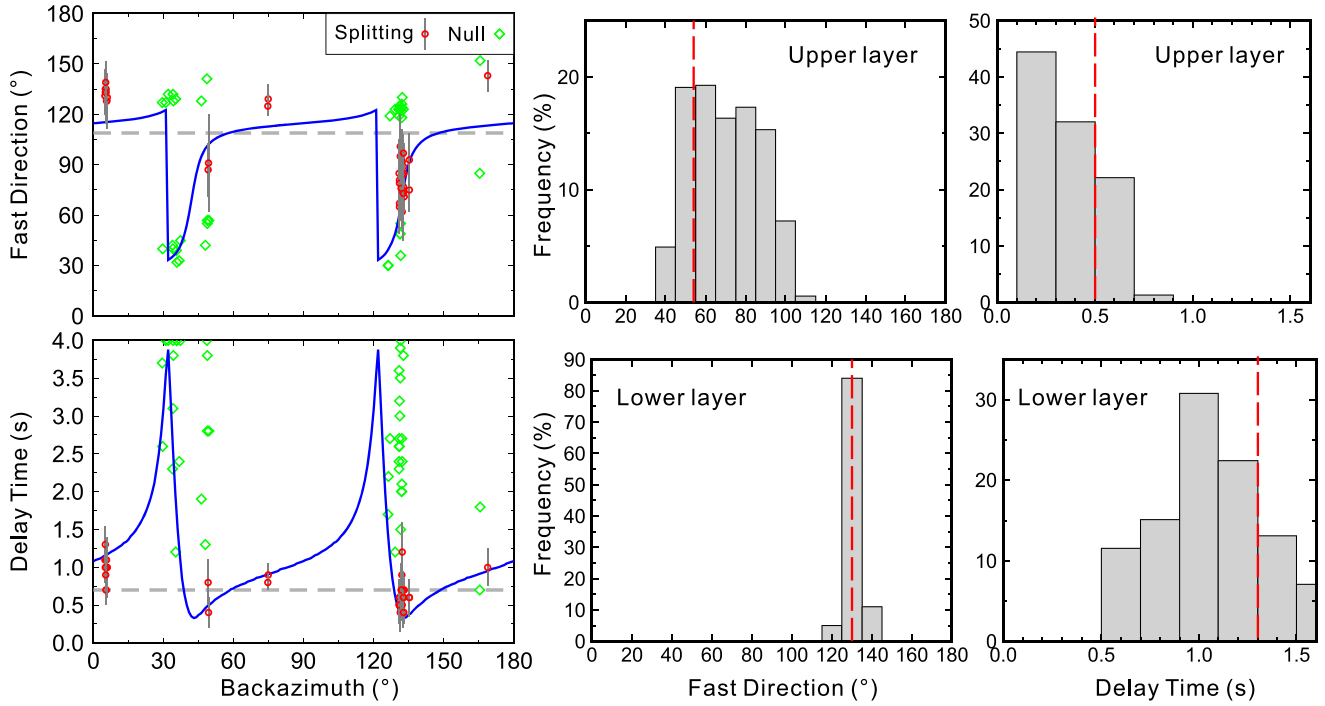

Figure 5. The two panels on the left show the variation of the two-layer anisotropy parameters (fast-wave direction and delay time) with the event backazimuth. The blue solid lines represent the theoretical splitting parameters obtained from the optimal two-layer anisotropy model ($\varphi_{upper} = 54^{\circ}$, $\delta t_{upper} = 0.5$ s, $\varphi_{lower} = 130^{\circ}$ and $\delta t_{lower} = 1.3$ s). Red dots with error bars indicate apparent splitting results. Green diamonds indicate null measurements. Horizontal grey dashed lines indicate average splitting values. The four histograms on the right show the distribution of the splitting parameters for the upper and lower layers. These were obtained from 3675 models and for an index $R > 0.25$. Red dashed lines indicate the optimal fast-wave direction and delay time values for the upper and lower layers (given above).

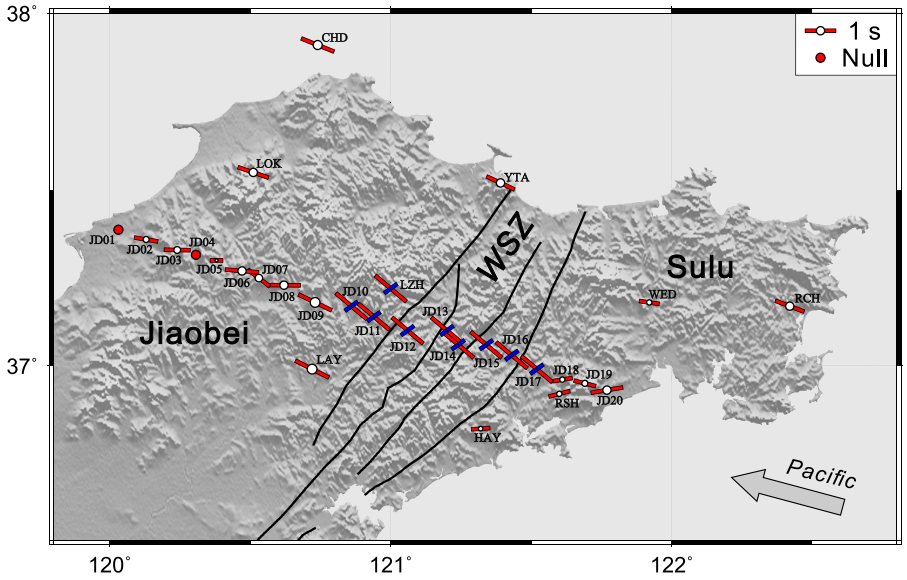

Figure 6. Station-averaged anisotropy results for the Jiaodong Peninsula (red bars of different length). A two-layer model allows estimating anisotropy in the WSZ: blue bars represent the splitting parameters for the upper layer, while red bars are the splitting vectors for the lower layer. Red dots mean null measurements. The scale for delay times is included in the upper right corner. The grey arrow indicates the subduction direction of the Pacific plate.

anisotropy as deriving mainly from the asthenosphere. However, fast directions are also generally parallel to trends in regional Late Mesozoic–Cenozoic extensional features. This indicates the contribution from lithospheric deformation could not be completely eliminated.

The E-W or WNW-ESE direction of the lower layer and one-layered anisotropy (Fig. 6) are consistent with results reported by previous studies of eastern China (Shi *et al.* 2015; Tian & Santosh 2015). Features appear roughly parallel to the subduction direction of the Pacific plate calculated using the GSRM V2.1 model

(Kreemer *et al.* 2014). The present northwestward subduction of the Pacific plate may thus cause asthenospheric return flow and corresponding anisotropy. Traveltime tomographic studies (Huang & Zhao 2006; Zhao *et al.* 2007) indicate that the subducted Pacific slab has stagnated within the mantle transition zone and underlies the entire region beneath eastern China. Deep-seated slab dehydration processes cause upwelling of high temperature asthenosphere materials and convective circulation in the mantle wedge as outlined in the big mantle wedge (BMW) model (Zhao *et al.* 2007). High temperatures reduce asthenospheric viscosity. This in turn enables LPO development to generate the anisotropy (Karato *et al* 2008). The anisotropy west of the Jiaobei massif is relatively weak (JD01–JD05, Fig. 6). These stations are located near the TLF (Fig. 1), which may have acted as a channel for asthenospheric upwelling during Late Mesozoic–Cenozoic continental extension and lithosphere thinning in eastern China (Chen *et al.* 2006; Zheng *et al.* 2008). A vertically flowing asthenosphere should induce a vertical olivine lineation, carried by the [100] crystal axes and therefore a small anisotropy for vertically propagating shear waves such as SKS waves (Ismail & Mainprice 1998). Zhao & Xue (2010) made similar observations about the NCC.

The anisotropy of the upper layer in the WSZ is oriented in a NE direction parallel to the strike of the WSZ (Fig. 6) implying a lithospheric cause of anisotropy. The collision between the NCC and SCB in the Jiaodong Peninsula during the Late Triassic led to coherent vertical deformation between the crust and lithospheric mantle at the suture zone to generate the LPO of anisotropic minerals parallel to the suture between the NCC and SCB. This caused the anisotropic NE oriented fast direction we observed. Anisotropy in the upper crust (∼15 km depth) is often caused by stress-aligned, fluid-filled cracks in the brittle crust (Crampin & Peacock 2005). This makes only a negligible contribution to the overall delay time in SKS-splitting. Anisotropy in the lower crust and upper mantle of ancient orogens in general is controlled by anisotropic minerals and may result from ductile deformation, dynamic recrystallization and annealing (Meissner *et al.* 2002), which is preserved as the fossilized anisotropy. The expression $L = (\delta t * V_s)\, A^{-1}$ (Bonnin *et al.* 2010), which links delay time δt (0.5 s), velocity of the shear wave (here SKS) V_s (mean value 4.0 km s^{-1}), anisotropy magnitude A (4 per cent) and length of the anisotropic path L, indicates that the thickness of the anisotropic layer should be ∼50 km. This agrees well with thickness estimates for the lower crust and lithospheric mantle in the Jiaodong Peninsula. When foliation exhibits vertical or high dip angles such as those observed for the WSZ, the XKS wave runs roughly parallel to the foliation plane and the delay time is about 0.1–0.2 s per 10 km in lower crustal rocks (Barruol & Mainprice 1993). Thus, the crustal contribution to the delay time observed for the upper layer can reach 0.2–0.4 s given a lower crustal thickness of 20 km. Receiver function analysis of the same profile with short-period dense stations shows a dislocation of the Moho on opposite sides of the WSZ. A wide-angle reflection/refraction study of the Jiaodong Peninsula by Pan *et al.* (2015) interpreted the WSZ as a major structural boundary because crustal velocity structures appeared different on either side of the suture zone. In the crustal detachment model (Li 1994), the upper crust of the SCB detached from the lower crust and thrust over the NCC into the Sulu region. Under these circumstances, deformation and any velocity contrast should be confined to the upper crust. Dislocation of the Moho therefore contradicts the crustal detachment model. Faure *et al.* (2001) argued that the boundary occurs north of the Sulu area based on the fact that the Jiaobei massif and Northern Sulu UHP massif experienced similar deformational episodes characterized by northwest extensional ductile deformation. However, structural analysis only captures upper crustal deformation which does not comport with the deeper deformation pattern obtained in this study. We therefore suggest that the WSZ represents a lithospheric-scale boundary. Intensive deformational fabrics likely record Late Triassic collision of the NCC and SCB and contrast deformational features of surrounding areas.

Following the collision between the NCC and SCB, the WSZ experienced significant Late Jurassic left-lateral movement on the scale of about 30 km. Additional right-lateral movement occurred from the Late Cretaceous to the Palaeocene (Zhang *et al.* 2007). Shearing action associated with these processes would also induce strike-parallel LPO of anisotropic minerals. Major strike-slip faults are confined within the upper crust. In terms of possible widening of shear zones at depth, the regional extent of oriented minerals could reach dozens of kilometers in width perpendicular to the fault (Lockett & Kusznir 1982). The upper layer anisotropic zone of the WSZ for example extends to stations JD10 and LZH (Fig. 6). The lateral extent of the upper layer anisotropy agrees well with dimension of the San Andreas Fault system where the anisotropic layer associated with each fault in the system reaches about 40 km width at the base of the lithosphere (Bonnin *et al* 2010). In addition, it should be noted that from Early Cretaceous to Palaeocene time, the eastern NCC experienced destruction and significant thinning of the lithosphere caused by palaeo-Pacific plate subduction (Zhu *et al.* 2004; Yang *et al.* 2005; Zhu & Zheng 2009; Chen 2010; Lin & Wei 2018; Yang *et al.* 2018). The lithosphere was not entirely modified by this event and still preserves information on its previous deformational history in the form of fossilized anisotropy in the remnant lithosphere.

5 CONCLUSIONS

We performed SWS measurements on teleseismic data from an NW-SE oriented seismic profile in the Jiaodong Peninsula, eastern China. Regional differences in splitting parameters were identified beneath the peninsula. Anisotropic structures beneath the Jiaobei massif and Northern Sulu UHP massif can be explained by a single anisotropic layer model. In the WSZ, the azimuthal dependence of splitting parameters indicates a two-layer anisotropy model. The fast direction of the lower layer and one-layered anisotropy aligns in a WNW-ENE direction. This direction accords with the present-day direction of Pacific plate subduction and could be associated with asthenospheric return flow in the BMW caused by subduction. The upper layer of the WSZ exhibits an NE-SW fast direction which agrees well with the overall strike of the WSZ. This supports the interpretation that the lithosphere preserves fossilized anisotropy induced by the Late Triassic collision between the NCC and SCB. Taken together, these observations indicate that the WSZ represents a lithospheric-scale boundary between the NCC and SCB.

ACKNOWLEDGEMENTS

We appreciate the assistance of the IGGCAS Seismic Array Laboratory and the members of the NCISP9 field team who collected data for this study including Dr Guiping Yu, Dr Enbo Fan, Dr Guangli Zhang, Dr Haodong Zhang, Dr Fanchang Meng, Dr Minfu Huang and Dr Fan Zheng. We are grateful to Prof Tianyu Zheng, Prof Wei Lin, Prof Guang Zhu, Prof Jinhui Yang and Dr Lingtong Meng for the helpful discussions on the interpretation of our results. We thank the Data Management Center of the China National Seismic

Network at the Institute of Geophysics, China Earthquake Administration (SEISDMC, doi:10.7914/SN/CB), for providing seismic data from permanent stations. Helpful comments and suggestions from Prof José Badal, the editor Prof Jörg Renner and an anonymous reviewer greatly improved this paper. We gratefully acknowledge financial support for this research from the Chinese National Key Research and Development Program (2016YFC0600101) and the National Natural Science Foundation of China (41804058).

REFERENCES

Barruol, G. & Mainprice, D., 1993. A quantitative evaluation of the contribution of crustal rocks to the shear-wave splitting of teleseismic SKS waves, *Phys. Earth Planet. Inter.,* **78**(3−4), 281–300.

Bonnin, M., Barruol, G. & Bokelmann, G., 2010. Upper mantle deformation beneath the North American–Pacific plate boundary in California from SKS splitting, *J. geophys. Res.,* **115**(B4), .

Bowman, J.R. & Ando, M., 1987. Shear-wave splitting in the upper-mantle wedge above the Tonga subduction zone, *Geophys. J. Int.,* **88**(1), 25–41.

Cao, G., Wang, Z. & Zhang, C., 1990. Jiaonan terrane in Shandong, tectonic significance of the Wulian–Rongcheng boundary fault, *Geol. Shandong,* **6**(1), 1–14.

Chen, L., 2010. Concordant structural variations from the surface to the base of the upper mantle in the North China Craton and its tectonic implications, *Lithos,* **120**(1–2), 96–115.

Chen, L., Zheng, T. & Xu, W., 2006. A thinned lithospheric image of the Tanlu Fault Zone, eastern China: constructed from wave equation based receiver function migration, *J. geophys. Res.,* **111**(B9), .

Crampin, S. & Peacock, S., 2005. A review of shear-wave splitting in the compliant crack-critical anisotropic Earth, *Wave Motion,* **41**(1), 59–77.

Faure, M., Le Breton, N., Lin, W. & Monié, P., 2002. Where is the North China-South China block boundary in eastern China?: reply, *Geol. Soc. Am,* Inc., BOULDER, CO, USA, **30**(7),668.

Faure, M., Lin, W. & Le Breton, N., 2001. Where is the North China–South China block boundary in eastern China?, *Geology,* **29**(2), 119–122.

Faure, M., Lin, W., Monié, P., Le Breton, N., Poussineau, S., Panis, D. & Deloule, E., 2003. Exhumation tectonics of the ultrahigh-pressure metamorphic rocks in the Qinling orogen in east China: new petrological-structural-radiometric insights from the Shandong Peninsula, *Tectonics,* **22**(3),.

Fontaine, F.R., Barruol, G., Tommasi, A. & Bokelmann, G.H., 2007. Upper-mantle flow beneath French Polynesia from shear wave splitting, *Geophys. J. Int.,* **170**(3), 1262–1288.

Fontaine, F.R., Barruol, G., Kennett, B.L.N., Bokelmann, G.H.R. & Reymond, D., 2009. Upper mantle anisotropy beneath Australia and Tahiti from P wave polarization: implications for real-time earthquake location, *J. geophys. Res.,* **114**(B3), .

Gao, S.S., Liu, K.H. & Abdelsalam, M.G., 2010. Seismic anisotropy beneath the Afar Depression and adjacent areas: implications for mantle flow, *J. geophys. Res.,* **115**(B12), .

Gilder, S.A. *et al.*, 1999. Tectonic evolution of the Tancheng-Lujiang (Tan-Lu) fault via middle Triassic to Early Cenozoic paleomagnetic data, *J. geophys. Res.,* **104**(B7), 15365–15390.

Hacker, B.R., Ratschbacher, L., Webb, L., Ireland, T., Walker, D. & Shuwen, D., 1998. U/Pb zircon ages constrain the architecture of the ultrahigh-pressure Qinling–Dabie Orogen, China, *Earth planet. Sci. Lett.,* **161**(1–4), 215–230.

Hacker, B.R. *et al.*, 2000. Exhumation of ultrahigh-pressure continental crust in east central China: Late Triassic-Early Jurassic tectonic unroofing, *J. geophys. Res.,* **105**(B6), 13339–13364.

Huang, J. & Zhao, D., 2006. High-resolution mantle tomography of China and surrounding regions, *J. geophys. Res.,* **111**(B9, .

Ismail, W.B. & Mainprice, D., 1998. An olivine fabric database: an overview of upper mantle fabrics and seismic anisotropy, *Tectonophysics,* **296**(1–2), 145–157.

Karato, S.-i., Jung, H., Katayama, I. & Skemer, P., 2008. Geodynamic significance of seismic anisotropy of the upper mantle: new insights from laboratory studies, *Annu. Rev. Earth Planet. Sci.,* **36,** 59–95.

Kreemer, C., Blewitt, G. & Klein, E.C., 2014. A geodetic plate motion and Global Strain Rate Model, *Geochem. Geophys. Geosyst.,* **15**(10), 3849–3889.

Li, Z.-X., 1994. Collision between the North and South China blocks: a crustal-detachment model for suturing in the region east of the Tanlu fault, *Geology,* **22**(8), 739–742.

Lin, W. & Wei, W., 2018. Late Mesozoic extensional tectonics in the North China Craton and its adjacent regions: a review and synthesis, *Int. Geol. Rev.,* 1–29, .

Liou, J.G., Zhang, R.Y., Eide, E.A., Wang, X.M., Ernst, W.G. & Maruyama, S., 1996. Metamorphism and tectonics of high-pressure and ultra-high-pressure belts in the Dabie–Sulu region, China, in: Harrison, M.T. & Yin, A.(Eds.), *The Tectonics of Asia*. Cambridge University Press, Cambridge, UK, pp. 300–344.

Lockett, J. & Kusznir, N., 1982. Ductile shear zones: some aspects of constant slip velocity and constant shear stress models, *Geophys. J. Int.,* **69**(2), 477–494.

Long, M.D. & Van Der Hilst, R.D., 2005. Upper mantle anisotropy beneath Japan from shear wave splitting, *Phys. Earth Planet. Inter.,* **151**(3–4), 206–222.

Meissner, R., Mooney, W.D. & Artemieva, I., 2002. Seismic anisotropy and mantle creep in young orogens, *Geophys. J. Int.,* **149**(1), 1–14.

Nicolas, A. & Christensen, N.I., 1987. Formation of anisotropy in upper mantle peridotites—a review, in *Composition, Structure and Dynamics of the Lithosphere-Asthenosphere System,* pp. 111–123, eds. Fuchs, K. & Froidevaux, C. AGU, Washington, DC.

Niu, F. & Li, J., 2011. Component azimuths of the CEArray stations estimated from P-wave particle motion, *Earthq. Sci.,* **24**(1), 3–13.

Okay, A.I. & Celal Sengo¨r, A., 1992. Evidence for intracontinental thrust-related exhumation of the ultra-high-pressure rocks in China, *Geology,* **20**(5), 411–414.

Pan, S. *et al.*, 2015. Crustal velocity structure beneath Jiaodong peninsula and its tectonic implications, *Chin. J. Geophys.,* **58**(9), 3251–3263.

Savage, M., 1999. Seismic anisotropy and mantle deformation: what have we learned from shear wave splitting?, *Rev. Geophys.,* **37**(1), 65–106.

Scholz, J.R., Barruol, G., Fontaine, F.R., Sigloch, K., Crawford, W.C. & Deen, M., 2017. Orienting Ocean-Bottom Seismometers from P- and Rayleigh waves polarizations, *Geophys. J. Int.,* **208,** 1277–1289.

Schulte-Pelkum, V., Masters, G. & Shearer, P.M., 2001. Upper mantle anisotropy from long-period P polarization, *J. geophys. Res.,* **106,** 21917–21934.

Shi, Y., Gao, Y., Tai, L. & Fu, Y., 2015. The shear-wave splitting in the crust and the upper mantle around the Bohai Sea, North China, *J. Asian Earth Sci.,* **111,** 505–516.

Silver, P.G., 1996. Seismic anisotropy beneath the continents: Probing the depths of geology, *Annu. Rev. Earth Planet. Sci.,* **24**(1), 385–432.

Silver, P.G. & Chan, W.W., 1988. Implications for continental structure and evolution from seismic anisotropy, *Nature,* **335**(6185), 34.

Silver, P.G. & Chan, W.W., 1991. Shear wave splitting and subcontinental mantle deformation, *J. geophys. Res.,* **96**(B10), 16429–16454.

Silver, P.G. & Savage, M.K., 1994. The interpretation of shear-wave splitting parameters in the presence of two anisotropic layers, *Geophys. J. Int.* **119**(3), 949–963.

Tian, X. & Santosh, M., 2015. Fossilized lithospheric deformation revealed by teleseismic shear wave splitting in eastern China, *GSA Today,* **25**(2), 4–10.

Tian, X., Zhang, J., Si, S., Wang, J., Chen, Y. & Zhang, Z., 2011. SKS splitting measurements with horizontal component misalignment, *Geophys. J. Int.,* **185**(1), 329–340.

Walker, K., Bokelmann, G., Klemperer, S. & Bock, G., 2005. Shear-wave splitting around the Eifel hotspot: evidence for a mantle upwelling, *Geophys. J. Int.,* **163**(3), 962–980.

Wang, X., Chen, Q.F., Li, J. & Wei, S., 2016. Seismic sensor misorientation measurement using P-wave particle motion: an application to the NECsaids Array, *Seismol. Res. Lett.,* **87**(4), 901–911.

Wu, C., Xu, T., Badal, J., Wu, Z. & Teng, J., 2015. Seismic anisotropy across the Kunlun fault and their implications for northward transforming lithospheric deformation in northeastern Tibet, *Tectonophysics,* **659,** 91–101.

Wu, Y.B., Zheng, Y.F. & Zhou, J.B., 2004. Neoproterozoic granitoid in northwest Sulu and its bearing on the North China-South China Blocks boundary in east China, *Geophys. Res. Lett.,* **31**(7), .

Wüstefeld, A., Bokelmann, G., Zaroli, C. & Barruol, G., 2008. SplitLab: a shear-wave splitting environment in Matlab, *Comput. Geosci.,* **34**(5), 515–528.

Wu¨stefeld, A. & Bokelmann, G.t., 2007. Null detection in shear-wave splitting measurements, *Bull. seism. Soc. Am.,* **97**(4), 1204–1211.

Yang, J., Zhao, L., Kaus, B., Lu, G., Wang, K. & Zhu, R., 2018. Slab-triggered wet upwellings produce large volumes of melt: insights into the destruction of the North China Craton, *Tectonophysics,* **746,** 266–279.

Yang, J.-H., Wu, F.-Y., Chung, S.-L., Wilde, S.A., Chu, M.-F., Lo, C.-H. & Song, B., 2005. Petrogenesis of Early Cretaceous intrusions in the Sulu ultrahigh-pressure orogenic belt, east China and their relationship to lithospheric thinning, *ChGeo,* **222**(3–4), 200–231.

Yin, A. & Nie, S., 1993. An indentation model for the North and South China collision and the development of the Tan-Lu and Honam fault systems, eastern Asia, *Tectonics,* **12**(4), 801–813.

Zhai, M., Cong, B., Guo, J., Liu, W., Li, Y. & Wang, Q., 2000. Sm–Nd geochronology and petrography of garnet pyroxene granulites in the northern Sulu region of China and their geotectonic implication, *Lithos,* **52**(1–4), 23–33.

Zhang, S. & Karato, S.-i., 1995. Lattice preferred orientation of olivine aggregates deformed in simple shear, *Nature,* **375**(6534), 774.

Zhang, Y.Q., Li, J.L., Zhang, T. & Yuan, J.Y., 2007. Late Mesozoic kinematic history of the Muping-Jimo Fault Zone in Jiaodong Peninsula, Shangdong Province, East China, *Geol. Rev. (in Chinese),* **53**(3), 289–300.

Zhao, D., Maruyama, S. & Omori, S., 2007. Mantle dynamics of Western Pacific and East Asia: insight from seismic tomography and mineral physics, *Gondwana Res*., **11**(1–2), 120–131.

Zhao, L. & Xue, M., 2010. Mantle flow pattern and geodynamic cause of the North China Craton reactivation: evidence from seismic anisotropy, *Geochem. Geophys. Geosyst.,* **11**(7), .

Zheng, T., Zhao, L., Xu, W. & Zhu, R., 2008. Insight into modification of North China Craton from seismological study in the Shandong Province, *Geophys. Res. Lett.,* **35**(22), .

Zheng, X., Yao, Z., Liang, J. & Zheng, J., 2010. The role played and opportunities provided by IGP DMC of China National Seismic Network in Wenchuan earthquake disaster relief and researches, *Bull. seism. Soc. Am.,* **100**(5B), 2866–2872.

Zheng, Y.-F., Zhou, J.-B., Wu, Y.-B. & Xie, Z., 2005. Low-grade metamorphic rocks in the Dabie-Sulu orogenic belt: a passive-margin accretionary wedge deformed during continent subduction, *Int. Geol. Rev.,* **47**(8), 851–871.

Zhou, J.-B., Wilde, S.A., Zhao, G.-C., Zheng, C.-Q., Jin, W., Zhang, X.-Z. & Cheng, H., 2008. SHRIMP U–Pb zircon dating of the Neoproterozoic Penglai Group and Archean gneisses from the Jiaobei Terrane, North China, and their tectonic implications, *PreR,* **160**(3–4), 323–340.

Zhu, G., Wang, D., Liu, G., Niu, M. & Song, C., 2004. Evolution of the Tan-Lu fault zone and its responses to plate movements in west Pacific basin, *Chin. J. Geol.,* **39**(1), 36–49.

Zhu, R. & Zheng, T., 2009. Destruction geodynamics of the North China Craton and its Paleoproterozoic plate tectonics, *Chin. Sci. Bull.,* **54**(19), 3354—3366.

SUPPORTING INFORMATION

Supplementary data are available at *GJI* online.

Figure S1. Sensor misorientation angles for the stations of the seismic array (red broken line) with reference to the number of earthquakes used for analysis (green broken line). The angles determined for the 20 temporary broad-band stations are around an average angle of −9.6° (deep blue solid line).

Figure S2. Individual XKS splitting measurements (red bars). The abbreviations are the same with those in Fig. 1.

Figure S3. Null SWS measurements in the study area. The red bars indicate the backazimuths of the incoming waves.

Table S1. The misorientation angles of the stations in this study.

Table S2. Average splitting measurements of stations with single-layer anisotropy.

Table S3. Individual splitting parameters and respective errors calculated for each station.

Please note: Oxford University Press is not responsible for the content or functionality of any supporting materials supplied by the authors. Any queries (other than missing material) should be directed to the corresponding author for the paper.